Pore scale 3D modelling of heat and mass transfer in the gas diffusion layer and cathode channel of a PEM fuel cell

A. Kopanidis [a], A. Theodorakakos [b], M. Gavaises [c], D. Bouris [a,*]

[a] Dept. of Mechanical Engineering, University of Western Macedonia, Bakola & Sialvera, 50100 Kozani, Greece
[b] Fluid Research Co, Harilaou Trikoupi 25, 10681 Athens, Greece
[c] City University London, Northampton Square, EC1V 0HB London, UK

A B S T R A C T

Flooding of the gas diffusion layer (GDL) of proton exchange membrane (PEM) fuel cells can be a bottleneck to the system's e f ficiency and even durability under certain operating conditions. Due to the small scale and complex geometry of the materials involved, detailed insight into the pore scale phenomena that take place are difficult to measure or simulate. In the present effort, a direct 3D microscale model of a portion of the PEM cathode channel and carbon cloth GDL is used to para-metrically investigate local heat and fluid flow at the GDL's pore scale and their effects on condensation of water vapour that leads to flooding. The 3D simulation through the microscale geometry is among the first appearing in the international literature. The Navier–Stokes, energy and water vapour transport equations are solved at steady state and in three-dimensional space for a range of inlet velocities and cloth fibre material properties, using a conjugate heat transfer approach to calculate the temperature field within the solid fibres. Psychrometric calculations are applied to provide indications of the conditions and areas most prone to condensation based on the calculated local temperatures and water vapour concentration.

*Keywords:*PEM fuel cell, CFD, Carbon cloth, Pore scale geometry Water vapour transport

1. Introduction

Fuel cells are a rapidly developing energy technology which offers major advantages and a broad range of applications in stationary and mobile systems. Its concept lies in the conversion of chemical energy to electricity in a series of fuel cell types for which different reactants and operating conditions apply e.g. Solid Oxide Fuel Cells (SOFCs) and Proton Exchange Membrane (or Polymer Electrolyte Membrane-PEM) fuel cells. In all cases, it has been observed that, at certain operating conditions, parts of the fuel cells may behave as bottlenecks to the whole system's efficiency and even durability. Characteristic examples are the formation of "hot spots" or "flooding" in the gas diffusion layer of the PEM fuel cell. These phenomena primarily appear at the micro or pore scale of the involved materials and detailed in situ insight into the physical mechanisms is rarely possible. Notable exceptions are recent works involving neutron radiography [1,2,3] which implements the transparency to neutrons of common materials such as aluminium as opposed to the attenuating properties of hydrogenous materials, such as water. However, the cost and effort required for implementation of these techniques still justifies exploration of other approaches. The present study is one of the first appearing in the international literature where the geometry at the pore scale of the Gas Diffusion Layer (GDL) is included in a 3D numerical simulation of the flow and heat transfer in a PEM fuel cell.

Numerous works have dealt with the flow in PEM channels, at a macroscopic level, both experimentally and numerically. Grujicic and Chittajallu [4] found that the optimum PEM cathode geometry is associated with parameters which promote the role of convective oxygen transport to the membrane-catalyst–cathode interface, reduce the thickness of the boundary diffusion layer and lower the possibility for cathode flooding. Quan and Lai [5] have numerically studied the air flow in the cathode channel for various operating conditions with the channel geometry and air inlet velocity as parameters. They found that hydrophilic surfaces increase pressure drop and that two-phase pressure drop inside the air flow channel increases almost linearly with increasing air velocity. A similar study was conducted for various channel geometries by Kumar and Kolar [6], who found that large values of channel heights lead to favourable conditions for flooding. Su et al. [7] have conducted

* Corresponding author. Tel.: +30 24610 56675; fax: +30 24610 56676.
E-mail addresses: tkopanidis@uowm.gr (A. Kopanidis), andreas@fluid-research.com (A. Theodorakakos), M.Gavaises@city.ac.uk (M. Gavaises), dmpouris@uowm.gr, dmpouris@uowm.gr (D. Bouris).

studies concerning flooding in PEM fuel cell cathode channels, finding that flooding mostly occurs downstream in the serpentine inter-digitated structures and typically at the corners of the channels. This suggests that the design of the path of the flow field should be streamlined in order to decrease the corner effect. Nguyen et al. [8] presented a three-dimensional computational fluid dynamics model of a PEM serpentine flow channel which, along with a voltage-to-current algorithm, calculates convective and diffusive heat and mass transfer along with local activation overpotential. In terms of temperature effects and water management, Zong et al. [9] developed a water and thermal management model for PEM fuel cells comparing results from uniform and non-uniform stack temperature models while Khandelwal and Mench [10] calculated the temperature difference across the thickness of a PEM fuel cell's porous GDL. Water management has been an object of thorough research [11,12] since it is crucial with regard to the performance of a PEM fuel cell. Most studies focus on the impact of the materials and operating conditions on the condensation phenomena taking place at the cell's cathode. Quick et al. [12] also quantified and modelled the vapour-water to air diffusion coefficients through experimental measurements and Siegel et al. [13] introduced a 3D model of the catalyst layer as an agglomerate instead of an homogenous material. There have also been a few experimental studies of the behaviour of water droplets on the surface of common GDL materials and in the channel under the influence of air flow [14,15,16]. However, most of the attention has been directed towards the formation of liquid water above the GDL and in the channel rather than the phenomena at the catalyst layer above the membrane and through the GDL. Finally, there have been attempts at experimental studies of the flow within fuel cell channels, such as the one by Yoon et al. [17] using PIV techniques, but their interest was again focused more on the 180° channel bends rather than the GDL itself.

In all of the cases mentioned above, the physical phenomena at the GDL were approached macroscopically, i.e. either by using the Darcy pressure drop relation as a source term in the momentum equations or by directly measuring macroscopic effects. Since the GDL is usually made of either carbon cloth or carbon paper, both being porous media that are considered to follow Darcy's law, this approach is acceptable but it provides limited insight regarding the details of the flow and temperature field inside the GDL. Only very recently have some publications appeared where the 3D geometry of the GDL microstructure is numerically reconstructed and included in the analysis. Mukherjee and Wang [18] and Kasula et al. [19] stochastically reconstructed a fibrous GDL from 2D electron microscopy while Innoue et al. [20] and Park et al. [21] modelled the GDL as randomly distributed straight cylinders.

The present effort continues in this direction by including a 3D model of the micro/pore-scale geometry of a portion of the PEM cathode channel and woven carbon cloth GDL in a 3D numerical simulation. This is the first time a woven carbon cloth is directly modelled at the pore scale as a part of a numerical study to parametrically investigate the heat and mass transfer induced under various operating conditions. The main objective is to make a connection between the pore scale geometry, the local heat and fluid flow and the condensation of water vapour that leads to flooding. Spatial discretisation is performed with a 3D unstructured tetrahedral mesh for both the gas phase as well as the solid fibres, in a conjugate solution of the temperature equation. The steady state momentum, continuity, energy and water vapour conservation equations are numerically solved using a SIMPLE-based algorithm. This is similar to previous work [22] where vapour phase transport was not considered and the effect of temperature and flow field could only be assumed. Quick et al. [12], state that although capillary and/or convective liquid water transport may (and usually does) exist in the GDL, it is evaporation and water vapour transport that is the dominant transport mechanism. The focus of the present work is on the water vapour transport and it is shown that the representation of the pore scale structure combined with a computational fluid dynamics (CFD) solution of a representative portion of the macro scale geometry can be used to realistically simulate macroscopically observed characteristics. Numerical results are obtained with regard to channel pressure drop and convective heat transfer and their effect on heat and mass transfer within the porous GDL is evaluated. Parametric studies are performed concerning entrance flow velocity, fibre temperature (constant or variable through its solid interior) and fibre material properties. This provides pore scale details for comparison and a better understanding of the heat and mass transfer phenomena, including condensation potential.

2. Modelling approach

The heat and mass transfer through a portion of the cathode channel and the carbon cloth GDL of a PEM fuel cell is considered. Initially, a 3D geometrical model of the carbon cloth, including individual fibres, and the overlying cathode channel was created. The whole domain was spatially discretised with an unstructured tetrahedral mesh in order to directly solve the Navier–Stokes and Energy equations, using boundary and operating conditions that will permit investigation of water condensation. The GDL is the part of a PEM fuel cell through which one of the reactants is convected and diffused from the channel towards the membrane and the catalytic substrate, where the reaction takes place (Fig. 1). Here, the dimensions of the cathode channel were chosen according to relevant international literature ([13,23]) and are denoted in Fig. 1b. PEM GDLs use either carbon paper or carbon cloth as the diffusing medium, taking advantage of their porous structure and chemical properties. The individual fibres of carbon cloths may be randomly strewn together or in the form of a well defined "knitted" structure [24] but this is not the case for carbon paper, whose topology is always random and difficult to be defined geometrically (Fig. 2). The "knitted" carbon cloth local topology was the material of choice for modelling in this work.

For reconstructing the geometry of the cloth, periodic repetition of a unit fibre cell was assumed (Fig. 3) in order to give the fibre structure that was included in the computational model (Fig. 1b). This unitary volume was initially created with the Wisetex software package for textile structure simulation [25] and then exported to a commercial 3D computer aided design (CAD) software in the form of a neutral file (IGES). The 4-fiber volume was scaled to dimensions that were in accordance with relevant measurements from a proprietary carbon cloth sample (Fig. 2b). In the present study, the compression of the carbon cloth within the fuel cell assembly has been assumed uniform, neglecting compression variation due to the more significant forces acting under the lands of the bipolar plate. Although this effect has been documented in the literature [26], including it here would have involved calculation of the structural deformation of the solid fibres, which goes beyond the scope of the study. However, rather than neglecting deformation altogether, it was assumed uniform across the cloth by taking the fibres' cross section to be elliptical thus accounting for tension between them and the overlying flow channel. The large axis of the elliptical fibre cross section was $d = 0.3$ mm, the space between parallel fibres in the large axis direction was $m = 0.4$ mm while the cloth's thickness, i.e. 2 fibres + void space perpendicular to the large axis of the elliptical cross section, was $Z_{th} = 0.38$ mm (Fig. 3).

The ratio of the void volume to the overall volume of a porous medium block is defined as the porosity ε of this medium:

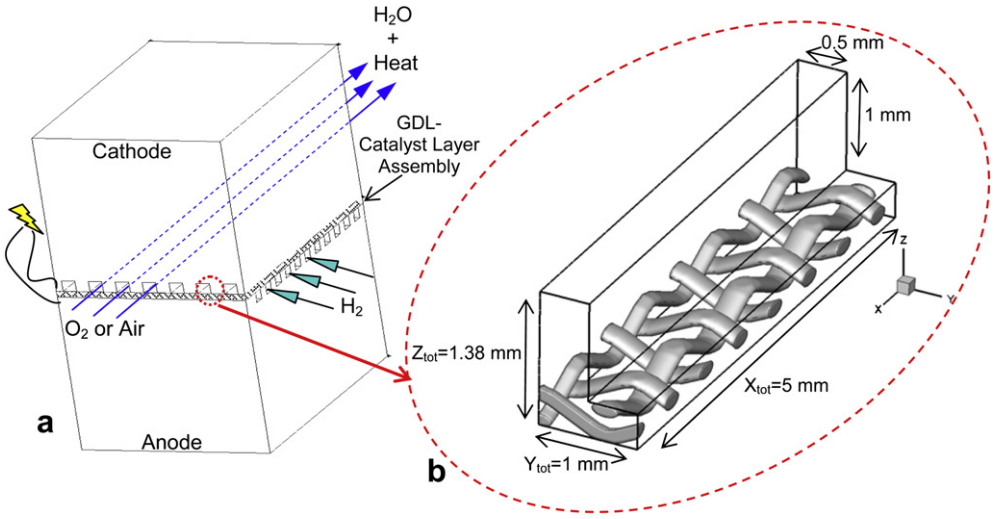

Fig. 1. a) Illustration of the Channel-GDL-Catalyst layer assembly in a PEM fuel cell, b) the computational domain of constructed GDL model.

$$\varepsilon = \frac{V_{tot} - V_s}{V_{tot}} \tag{1}$$

Actual cloth fibres are in turn made up of thinner fibres (Fig. 2b) and thus have a porosity of their own. In the present approach, each fibre is considered solid with no flow through it and a fibre porosity value of unity, while a basic weaving structure is applied rather than a random overlaying of fibres. However, care has been taken to preserve the overall porosity of the present woven carbon cloth model at $\varepsilon = 0.75$, which is in accord with common GDL media porosity values of 0.6–0.9 [24]. Of course, this implies that transport through the GDL is only possible between and not through the model's fibres. The full computational domain and final structure included the fibres and the channel, leaving the appropriate void space in the cloth (Figs. 1b and 3c). Based on the constraint that the overall porosity value is preserved, the major characteristics of the flow are expected to be relevant to the actual situation.

Solution of the flow field assumed steady state flow for the simulated operating conditions, so time derivatives are omitted from the equations presented. As far as the flow field is concerned, the Navier–Stokes and continuity equations are solved, for incompressible flow:

$$\vec{u} \cdot \nabla(\rho \vec{u}) = -\nabla P + \mu \nabla^2 \vec{u} \tag{2}$$

$$\nabla \cdot (\rho \vec{u}) = 0$$

where $(\vec{u})$ is the velocity vector, (P) is static pressure, (μ) is fluid dynamic viscosity and (ρ) is density, which varies depending on temperature alone. As the portion of the channel being studied is small, the conservation of mass does not take into account water vapour production and oxygen consumption along the computational domain. Reynolds number (*Re*) defines the kind of the flow field, since it gives a measure of the inertia forces to viscous forces ratio, thus characterising the field as laminar or turbulent. Here *Re* number is calculated based on hydraulic diameter (D_h):

$$\mathrm{Re} = \frac{D_h U_o \rho}{\mu}$$

$$\mathrm{D_h} = \frac{4\mathrm{A_{chan}}}{\mathrm{J}} \tag{3}$$

with U_o [ms^{-1}] being the mean (or inlet) air velocity, D_h [m] the hydraulic diameter, A_{chan} [m^2] the free path area (including the part filled with the carbon cloth) of the domain cross section and J [m] the cross-section's wetted perimeter.

For the temperature field, the energy equation is formulated assuming constant specific heat (C_p) but actually allows for local variation by solving for the value of (C_pT) instead of temperature alone:

$$\rho \vec{u} \nabla(C_P T) - \nabla \cdot \left[\frac{k}{C_P} \nabla(C_P T)\right] = S_\Phi \tag{4}$$

where (T) is temperature, (k) is thermal conductivity and S_Φ represents any possible heat source terms e.g. thermal source or due to viscosity. In the present case, viscous heat is negligible and there is no other heat generation, so $S_\Phi = 0$. The above system of equations is volume averaged on the unstructured tetrahedral volume mesh and then solved using a SIMPLE-based methodology [27]. The finite volume method was used for discretisation with hybrid upwind differencing for the convection terms and second

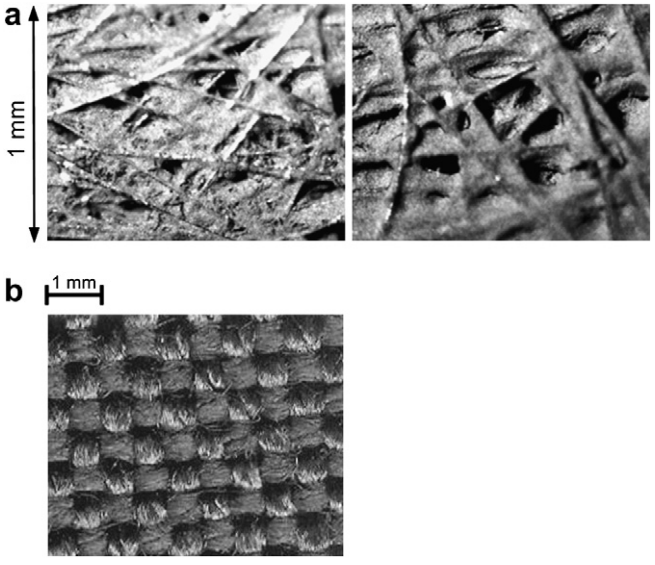

Fig. 2. a) Carbon paper photo b) Carbon cloth fibres' detail.

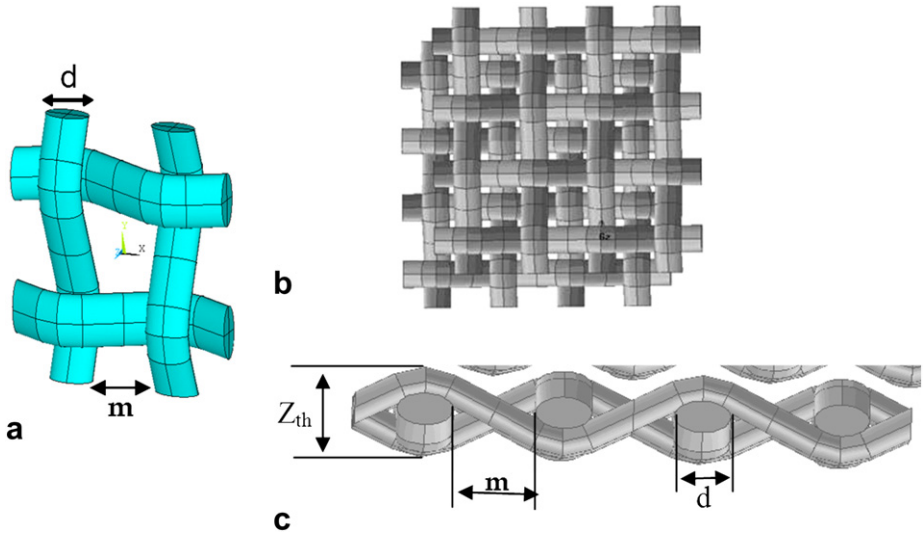

Fig. 3. a) Elementary volume structure, b) Reconstructed carbon cloth, c) Side view of cloth.

order central differencing for the diffusion and source terms. The code was not parallelised and convergence was assumed when equation residuals fell by at least three orders of magnitude and were also below 0.5% of incoming mass flow weighted values.

For the case of the conjugate solution inside the fibres, the temperature at the common fibre-fluid boundary should be given by the equation [28]:

$$T_{S-F} = \frac{ck_s T_s + k_f T_f}{ck_s + k_f} \tag{5}$$

where $T_{S\text{-}F}$ is the temperature at the common boundary, T_S is the temperature of the solid phase, T_f is the fluid temperature and k_s and k_f the thermal conductivity of the solid and fluid respectively. Lastly, c is the ratio of the normal distance between the first mesh node and the solid-fluid boundary on the fluid (dy_f) and solid (dy_s) side (Fig. 4):

$$c = \frac{dy_f}{dy_s} \tag{6}$$

Finally, mass conservation for water vapour is expressed through the equation of transport for water vapour concentration Y_{H2O} [$kg_{H2O}kg_{gm}^{-1}$]:

$$\rho \vec{u} \nabla Y_{H2O} = \nabla \cdot (\rho D_{gm,H2O} \nabla Y_{H2O}) + S_{H2O} \tag{7}$$

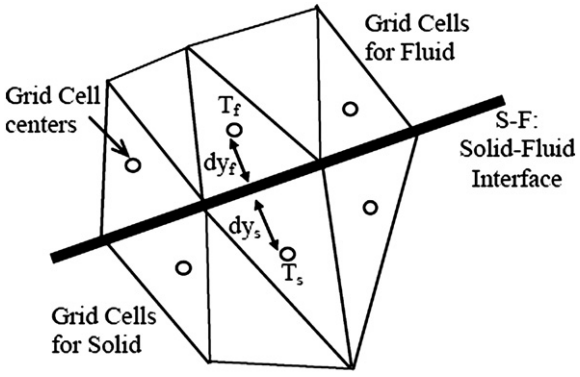

Fig. 4. Detail of local grid at the solid-fluid interface.

where the index "gm" indicates gas mixture and the source term S_{H2O} is the production rate of water vapour per unit volume. After volume averaging for the grid cell volume (V_{cell}). the source term becomes $\int_{V_{cell}} S_{H_2O} dV = \dot{m}_w \cdot A_{surf}$, where $\dot{m}_w$ is the water production per unit surface of catalyst-membrane layer and A_{surf} is the surface of the grid cell volume in contact with the water producing layer. Results regarding water vapour are presented in the form of relative humidity (φ), which determines proximity to saturation:

$$\varphi = \frac{P_W}{P_{WS}} \tag{8}$$

In (8), P_W is the vapour partial pressure while P_{WS} is the saturation pressure, both at the temperature of the mixture. Calculation of the saturation pressure as a function of temperature has been a subject of study for many years and numerous empirical correlations have been proposed for various temperature ranges. Bolton [29] suggests that

$$P_{WS} = 611 \cdot 10^{\frac{7.5T}{T+237.3}} \tag{9}$$

is acceptable except when extreme accuracy (>2%) is required at very low temperatures, in which case

$$P_{WS} = 611 \cdot e^{\frac{17.67T}{T+243.3}} \tag{10}$$

gives an accuracy of 0.1% between −30 °C and 35 °C. In the previous equations, T is the temperature in °C. There are high order polynomials [30] that can give better accuracy for a wider range of temperature values but for the present calculations, (9) was considered sufficient.

If the humidity ratio is defined as the ratio of the water mass and the dry air mass [$kg_{H2O}\ kg_{dry\ air}^{-1}$], then using their molecular weights and mole fractions (x) will give :

$$W = \frac{m_w}{m_{da}} = \frac{18.01528 \cdot x_w}{28.9645 \cdot x_{da}} = 0.62198 \frac{x_w}{x_{da}} \tag{11}$$

Assuming ideal gas behaviour, the mole fraction is equal to the ratio of partial pressure to total pressure and (11) gives:

$$P_W = \frac{W \cdot P}{(0.62198 + W)} \tag{12}$$

with P being the static pressure of the mixture [Pa]. The relative humidity can now be calculated from the mixture's local pressure, temperature and humidity ratio:

$$\varphi = \frac{\frac{W \cdot P}{(0.62198 + P)}}{611 \cdot 10^{\frac{7.5T}{T+237.3}}} \quad (13)$$

Further details and a concise analysis of basic psychrometric calculations can be found in [31] and [32].

Since there is a local variation of the gas mixture quality i.e. due to humidity production, the values of mixture density, viscosity and specific heat appearing in eqs. (2), (4) and (7) are calculated based on the molecular weight and local humidity concentration. However, due to the short length of the computational domain, mass variations due to humidity production and oxygen consumption are neglected and therefore the equation of continuity (2) is applied for the whole mixture without any sources or sinks.

3. Boundary and operating conditions

For the computational domain shown in Fig. 1b, the flow is always in the x direction, the catalyst layer above the membrane is on the $Z = 0$ plane, $Y = 0$ and $Y = Y_{tot}$ are symmetry planes and all other outer surfaces are solid adiabatic walls. Several researchers report operating conditions for PEM fuel cells [5,33,34]. In this study, all calculations were performed assuming a constant and uniform inlet air distribution with values ranging between $U_o = 0.3$ and 8.4 ms^{-1}. Constant pressure boundary conditions were attempted, in order to simulate fully developed flow, but stagnation regions on the fibres just in front of the inlet led to convergence difficulties and the approach was abandoned. Other simplifications have also been applied here, most notably the adiabatic temperature boundary condition at the bipolar plate–channel interface. Defining the temperature field at the cathode channel walls has been a matter of discussion for some time and a variety of numerical approaches have been applied [35], including constant temperature and constant heat flux conditions, which have been deemed inappropriate [36]. On the other hand, most experimental approaches strive to maintain a uniform temperature distribution, i.e. isothermal conditions throughout the cell [2,3,37]. Typically, the bipolar plates would include a cooling circuit but in order to accommodate this in the present approach, the cooling channels would have to be included in the solid region of the plates and they would have to be solved using the conjugate heat transfer approach. Given the extensive computational demand of directly modelling the carbon cloth itself, this was prohibitive. Alternatively, prescribing a constant temperature or heat flux at the plates would significantly, and questionably, affect the area under the lands of the bipolar plates. In effect, the current approach neglects the effect of the bipolar plate on the temperature field (not the flow field) in the channel and the GDL. This is a conservative assumption with regard to the scope of the study since lower temperatures of the plates would facilitate condensation.

With regard to the boundary condition for the energy equation at the catalyst layer, in reality heat is mainly generated due to thermodynamic irreversibilities. However, solving at the pore scale of the carbon cloth, local variations in these reactions should be taken into account and a variable heat flux would arise along the catalyst layer. Chemical reactions are not included in the present simulations and therefore a simplification of constant heat flux or constant temperature must be chosen. For the short channel length being simulated, a constant temperature boundary condition was considered sufficient for the present study.

Finally, another point worth mentioning in regard to the flow field is the fact that when multiple neighbouring channels are considered i.e. as part of a serpentine, it has been documented that certain flow conditions may lead to a by-pass of the channel and mixing of the flows in neighbouring channels [41]. This is, of course, an undesirable condition and understanding of the phenomenon is of value in order to avoid it but for its inclusion in a simulation of channel flow, at least two channels must be included in the geometry. This increases computational effort and has not been included in the present study.

After the topology of the computational domain was constructed, it was discretised with an unstructured mesh of $6.72 \cdot 10^5$ tetrahedral volume elements (Fig. 5). Mesh quality was checked for excessive skewness and then three further grids consisting of $2.72 \cdot 10^5$, $8.87 \cdot 10^5$ and $1.28 \cdot 10^6$ elements were constructed for grid independence confirmation. For the same entrance velocity (1.43 ms^{-1}), differences in calculated pressure drop per unit length were 1.77, 0.0, 0.08 and 1.02% in ascending order of the four grids' densities respectively, thus indicating mesh independency of the solution.

For heat transfer calculations, air inlet temperature was 293 K while the temperature at the catalyst layer was a constant 353 K. The inlet temperature is quite low for typical operating

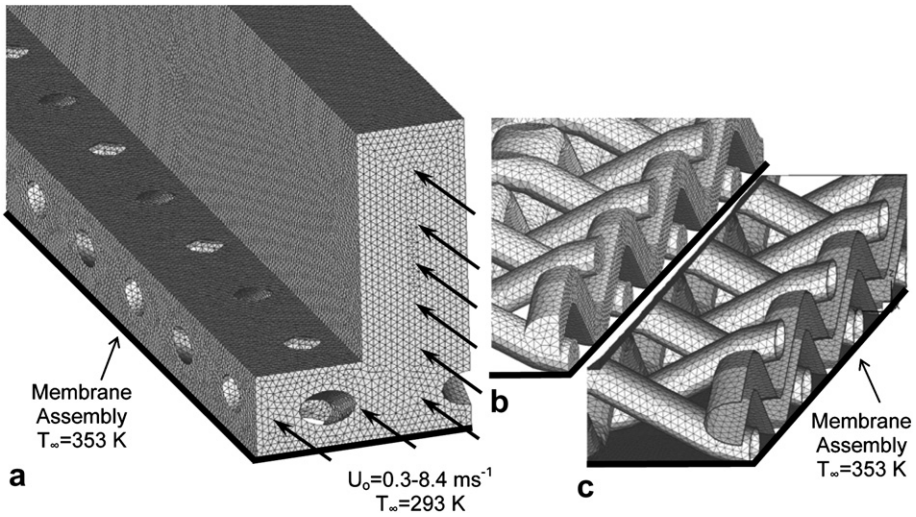

Fig. 5. a) Volume mesh for the void space of the computational domain b) volume mesh inside the solid fibres of the cloth (conjugate solution) c) surface mesh defining the fibres.

temperatures of a PEM fuel cell membrane [13,23] but may be considered relevant to start up conditions, before normal operating temperatures are attained. Fibre temperature was either solved conjugately with the flow or assumed at the same constant temperature as the catalyst ($T = 353$ K). In conjugate heat transfer solutions, spatial discretisation extended within the solid fibres (Fig. 5c), where two individual sets of physical properties were assigned to the fibre material: pure carbon/graphite ($k = 3$ W m^{-1} K^{-1}, $\rho = 1225$ kg m^{-3} and $C_P = 700$ J kg^{-1} K^{-1}) and a commercial ELAT® cloth ($k = 0.27$ W m^{-1} K^{-1}, $\rho = 330$ kg m^{-3} and $C_P = 610$ J kg^{-1} K^{-1}). These are within the wide range of effective thermal conductivities for typical carbon felts as documented by Ramousse et al. [38]. The thermal conductivity of graphite is much higher but the applied values are in accordance with the previously mentioned simplification that the fibres in the present model actually represent a composition of smaller fibres and therefore an effective thermal conductivity must be applied. The difference in axial and radial thermal conductivity has not been taken into account for the fibres and the larger value is expected to be closer to the actual fibre thermal conductivity [38]. Finally, although gravitational effects are included in the calculations, their effect is minor since the density driven buoyancy effects were found negligible compared to convection.

The present calculations consider only heat and fluid flow for a very small portion of a typical cathode channel length. Water vapour production, gas flow rate and cell voltage and power are all related but since electrical phenomena are not included in the present calculation, momentum and mass transfer parameters were chosen so that they are in agreement with the relevant parameters of the whole fuel cell system. Therefore, with regard to water vapour production and transport, production per unit membrane area was assumed constant at $\dot{m}_w = 4.66 \cdot 10^{-4}$ [kg_{H2O} s^{-1} m^{-2}]. Indicatively, this corresponds to a PEM fuel cell with 5 cm^2 membrane area, operating at a voltage of $V_e = 0.65$ V and producing $P_e \sim 1.6$ W. These values are in agreement with an available experimental configuration of a PEM fuel cell [39] and also the theoretical analysis for PEM FC water production $\dot{m}_{H_2O}$ [kg_{H2O} s^{-1}], according to Larminie and Dick [40]:

$$\dot{m}_{H_2O} = 9.34 \cdot 10^{-8} \frac{P_e}{V_e} \tag{14}$$

Since the pore scale simulation does not permit solving for the whole serpentine channel, a choice had to be made with regard to the values of relative humidity at the entrance of the computational domain. Larminie and Dick [40] state that the produced fuel cell power can be ideally expressed as :

$$P_c = V_c \cdot 4 \cdot F \cdot M_{O_2} \cdot \dot{m}_{O_2} \tag{15}$$

where $F = 96485.34$ [Cmol^{-1}] is Faraday's constant and M_{O2} is the molecular weight of Oxygen. Taking the molecular weight of air MB = 28.97 with 21% oxygen concentration by volume, the stoichiometric air requirement $\dot{m}_{air,stoich}$ [kg_{air} s^{-1}] becomes:

$$\dot{m}_{air,stoich} = 3.57 \cdot 10^{-7} \frac{P_e}{V_e} \tag{16}$$

and an air ratio can be defined as $\lambda = \dot{m}_{air}/\dot{m}_{air,stoich}$. For the present channel geometry and a 5 cm^2 fuel cell operating at atmospheric pressure with inlet velocities $U_o = 0.3$–8.4 ms^{-1}, the air ratio is $\lambda \approx 0.3$–10. It is reiterated that the purpose of the previous analysis is to put the present calculations of a small portion of the cathode channel length into perspective with regard to the fuel cell to which it belongs. The lowest velocity value, which gives an air-fuel ratio of $\lambda = 0.3$ for the 5 cm^2 fuel cell, is not realistic since it would lead to cathode starvation. However, for a smaller fuel cell

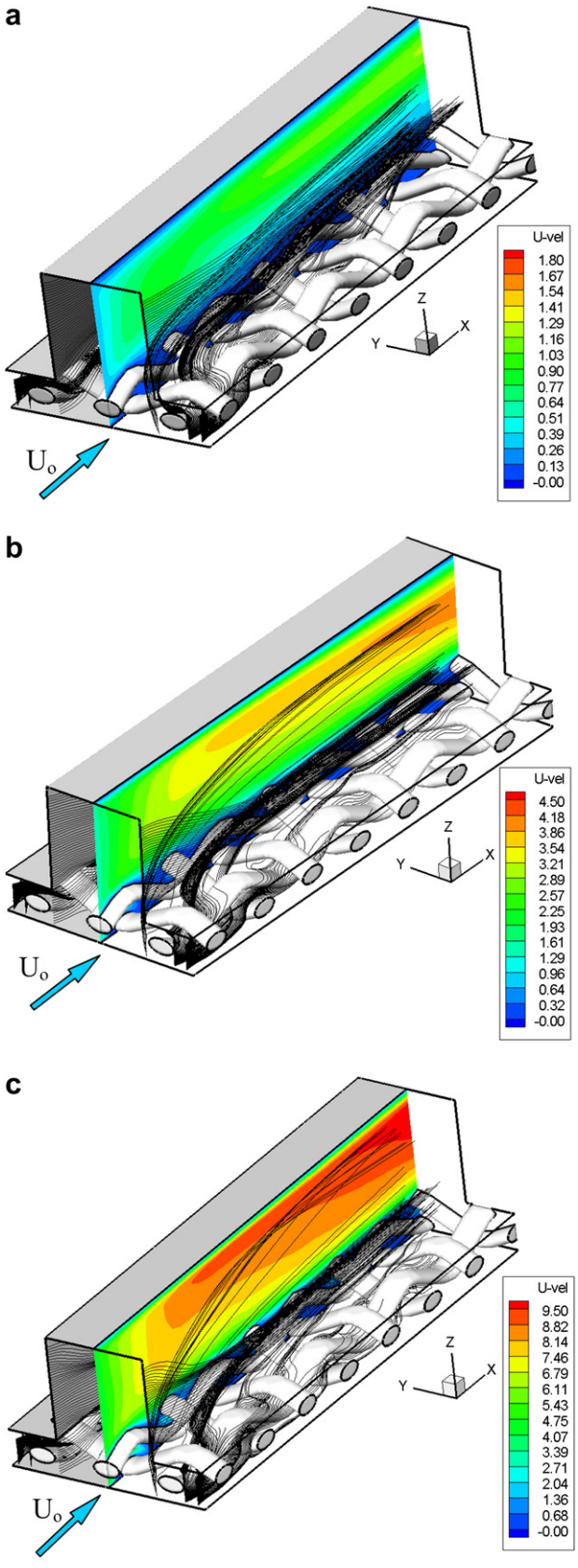

Fig. 6. Velocity distribution contours and streamlines inside the GDL and cloth computational domain for the cases of a) $U_o = 0.3$ ms^{-1}, b) $U_o = 1.43$ ms^{-1} c) $U_o = 4.29$ ms^{-1} as constant inlet velocities. (Domain has been mirrored across XZ plane and the bipolar plate walls removed, for clarity).

with a shorter channel length, it would correspond to an air-fuel ratio above unity and so results will be presented for the $U = 0.3$ ms^{-1} value, mostly for comparison purposes and to underline the effect of the flow velocity and momentum.

In agreement with the above mentioned values for air-fuel ratio and a typical total length of the cathode channel, the computational domain corresponds to a downstream portion of the cathode channel, where relative humidity levels have already risen to near saturation and are taken to be between 99 and 99.6%. Of course neither humidity nor velocity distributions will actually be uniform but, as will be shown in the results of the calculations, they do develop within a relatively short distance from the inlet so that reliable conclusions may be drawn.

4. Results

Initially, parametric studies were performed at isothermal conditions for a range of inlet velocities between 0.3 and 8.4 ms^{-1}, corresponding to laminar flow Reynolds numbers $Re_{Dh} = 14-400$. Since gravitational effects are negligible, the conclusions with regard to the flow field will not be influenced by the subsequent introduction of a temperature difference.

The non-dimensional pressure drop through the channel, expressed as the friction coefficient $f = D_h \Delta P / 0.5 \rho L U^2$, is higher by a factor of two compared to the well known $f = 64/Re$ law for laminar duct flow for all inflow velocity values except the lowest, which is in perfect agreement [28]. This is expected since the laminar duct flow law corresponds to the same channel configuration without the carbon cloth, whose presence obviously introduces an extra pressure drop and even more so at higher velocity values. Rawool et al. [41] made similar observations with porous transport layers of low permeability leading to higher pressure drop. A closer look at Figs. 6–8 supports this explanation. The higher inlet velocities force the flow through the carbon cloth where pressure drop is highest. The flow pathlines in Fig. 6 clearly show that for the lowest velocity value the flow quickly leaves the cloth fibre matrix and enters the channel while at higher velocities this is not as prominent. Contours of iso-velocity at two downstream planes perpendicular to the main flow direction are shown in Fig. 7. Velocity is presented in non-dimensional form to aid in the comparison and it is clear that higher velocities lead to a more uniform flow, possibly because the pressure drop in the channel becomes comparable to that of the lower velocities in the cloth. Velocity profiles taken at a position in between the planes of Fig. 7 are presented in Fig. 8 where it is obvious that the non-dimensional velocity profile within the cloth becomes self similar and fully developed at a much lower velocity than the channel flow. These results are in agreement with those of Grujicic and Chittajallu [8] who found that increased oxygen transport to the catalyst/cathode interface and reduction of the thickness of the boundary layer are prerequisites for optimum PEM cathode geometry and may help to minimise flooding. It is shown here (Figs. 6–8) that higher inflow velocities will facilitate this and should further help with the removal of the water vapour that is produced.

The effect of temperature on fuel cell operation has been documented in the past for a large range of operating temperatures (303–353 K) [42]. Here, taking advantage of the fibre-scale simulation, the investigated parameters have been extended towards the effect of the cloth fibres' material properties. Although calculations have been performed for common inlet temperatures of $T = 353$ K and $T = 333$ K [43], heat transfer results are presented for inlet temperatures equal to ambient ($T = 293$ K) - a situation that

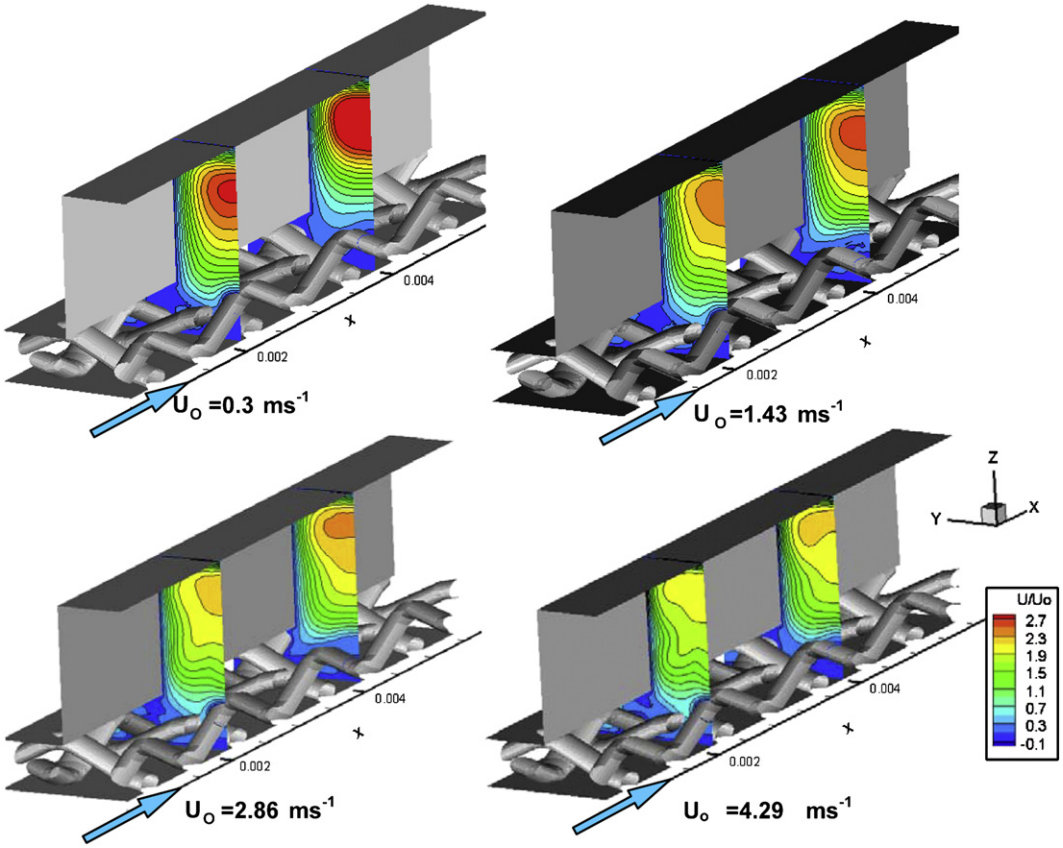

Fig. 7. Dimensionless velocity contours for various entrance velocities at ($X/X_{tot} = 0.4$) and ($X/X_{tot} = 0.8$).

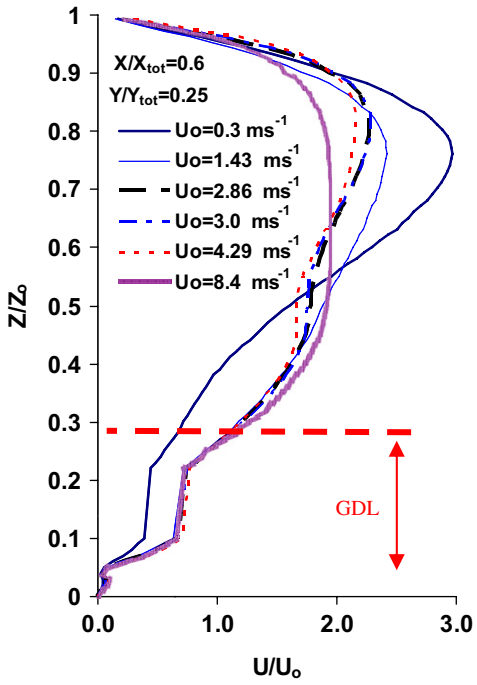

Fig. 8. Dimensionless velocity profiles at the channel mid-section ($Y/Y_{tot} = 0.25$) through the GDL and the height of the channel for various entrance velocities. The GDL thickness from $Z/Z_{tot} = 0$ to $Z/Z_{tot} = 0.27$ is marked on the figure for clarity.

will only arise during the transient start up period—in order to underline the effect. The base case has been that the fibres assume the same temperature as the catalyst ($T = 353$ K) but conjugate solutions of the temperature field in the flow and in the solid fibres have also been performed for two different fibre materials.

The temperature field on the surface of the fibres and a plane midway along the channel (Y/Y_{tot}) is portrayed in Fig. 9. Fig. 9a shows the case when the fibre temperature is imposed equal to that of the catalyst ($T = 353$ K) and Fig. 9b shows the same regions when the temperature field in the solid fibres is solved for ELAT material properties. The result shows much lower temperatures within the region of the GDL although the effect does not manage to reach the upper part of the channel in the length of the computational domain. However, the fibre temperatures seem to increase downstream so that, given a long enough channel, a situation resembling that in Fig. 9a may eventually be attained. In any case, the effect of the fibre material properties is evident within this developing region. This is better quantified in Fig. 10 where the mean air outflow temperature is presented for three configurations and a range of inlet air velocity values. The three configurations are: i) constant fibre temperature assumption ($T = 353$ K), ii) conjugate temperature solution through fibre material assuming ELAT carbon cloth properties and iii) conjugate temperature solution through fibre material assuming pure carbon (graphite) properties. It is obvious that the conjugate solutions result in consistently lower outflow temperatures compared to the assumption of constant fibre temperature. Specifically, the commercial cloth properties (ELAT) lead to lower outflow temperature and are more sensitive to convective effects i.e. higher inlet velocities lead to larger temperature variations. In all cases however, an asymptotic state appears for high velocities, where convection can be considered dominant.

In Fig. 11, the mean temperature on a plane parallel to the membrane—separating the GDL from the channel—has been calculated for the two different fibre properties and a range of inlet velocities to give the temperature differences between the catalyst

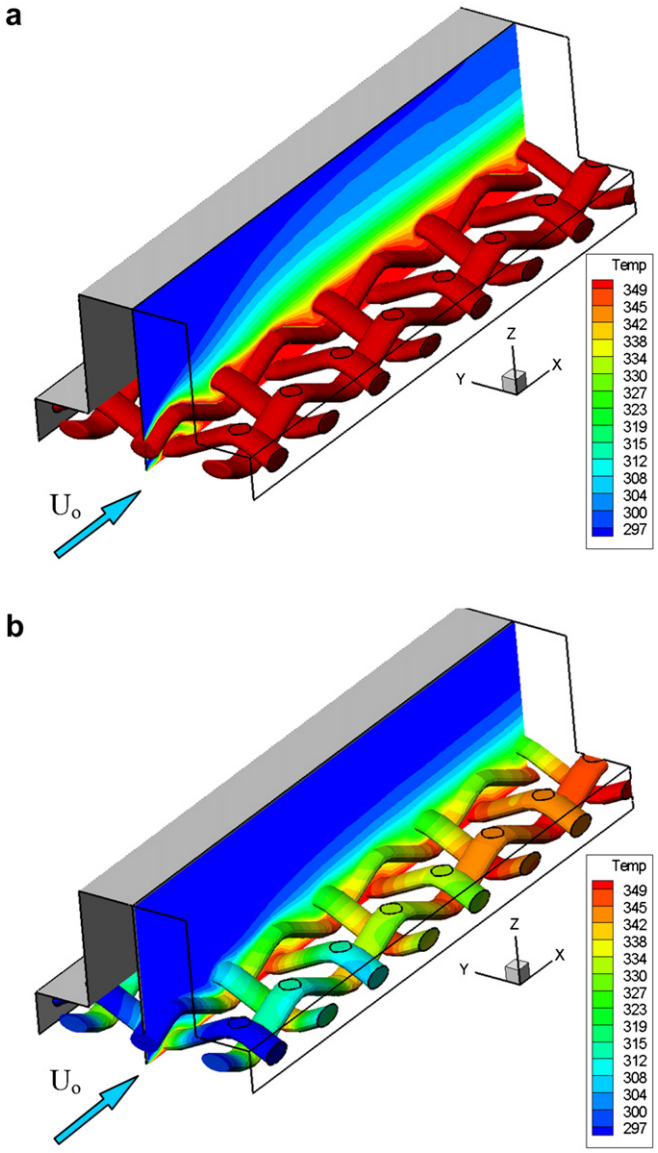

Fig. 9. Contours of constant temperature on the fibres and an XZ plane at $Y/Y_{tot} = 0.25$ for $U_o = 8.4$ ms^{-1}. a) Constant temperature imposed at fibres' surface, b) Conjugate temperature solution through the solid fibres with the properties of carbon cloth (ELAT). (Domain has been mirrored across XZ plane and the bipolar plate walls removed, for clarity).

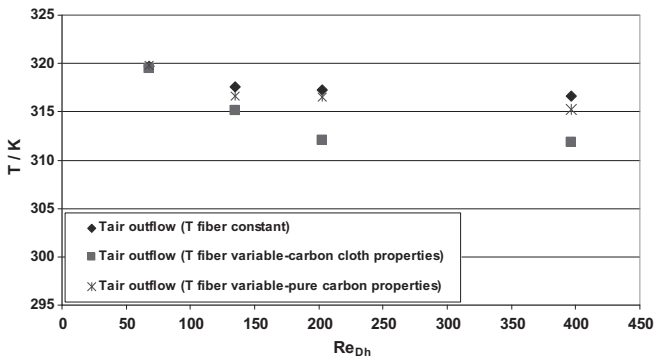

Fig. 10. Outflow air temperature for constant temperature at fibres, variable fibre temperature for commercial carbon cloth properties (carbon cloth) or graphite (pure carbon) properties.

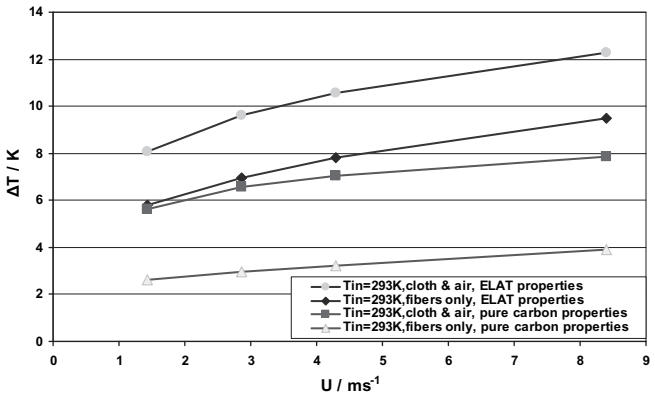

Fig. 11. Mean temperature values between PEM catalyst layer ($\Delta T = T_{Cat} - T_{Local}$, $T_{Cat} = 353$ K) and the top of the GDL for the fibres and the mean plane temperature (fibre and air).

and the top of the GDL. Here, mean temperatures were calculated for both the fibre material in the plane as well as the whole plane (fibres + air). From the present results in the region where flow is developing, temperature variation within the GDL seems to reach values >10–12 K while Khandelwal and Mench [10] expect temperature variations of 7–8 K in diffusion media of the present thickness. This may be explained by the fact that much larger lengths were examined there and is in agreement with Fig. 9, where the temperature differences in the cloth are smaller as the flow progresses downstream.

Based on psychrometric processes [31] and for the calculated mean flow temperature at atmospheric pressure, the humidity concentration values at which 100% relative humidity (i.e. potential condensation) is attained are plotted in Fig. 12 for a range of inlet velocities and the three fibre conditions (constant temperature, ELAT and carbon properties). The resulting difference of over 30% in the "condensing" humidity ratio for different fibre properties and the same flow velocity underlines the importance of the heat transfer mechanisms in the GDL.

During operation of a PEM fuel cell, the reaction taking place at the catalyst is assumed to produce water vapour and not liquid [40,44,35]. Following the numerical simulation of heat and fluid flow in the GDL, the final effort of this work focused on water vapour production, vapour mass transport and psychrometric interaction with the temperature field in an attempt to obtain indications of potential water vapour condensation. A range of inlet air velocities (0.3–4.3 ms^{-1}), temperatures (293–353 K) and relative humidity (40–99.6%) values were applied while the two sets of

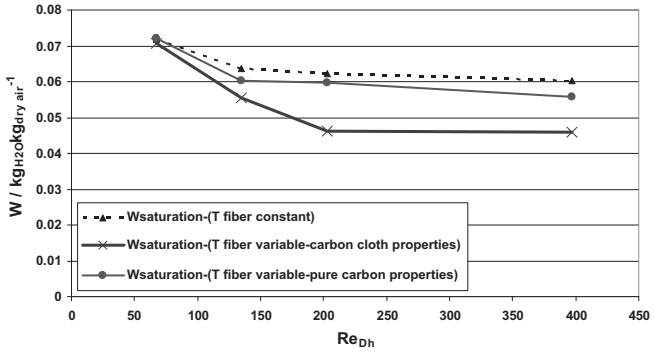

Fig. 12. Humidity ratio leading to condensation for each outflow temperature of Fig. 10.

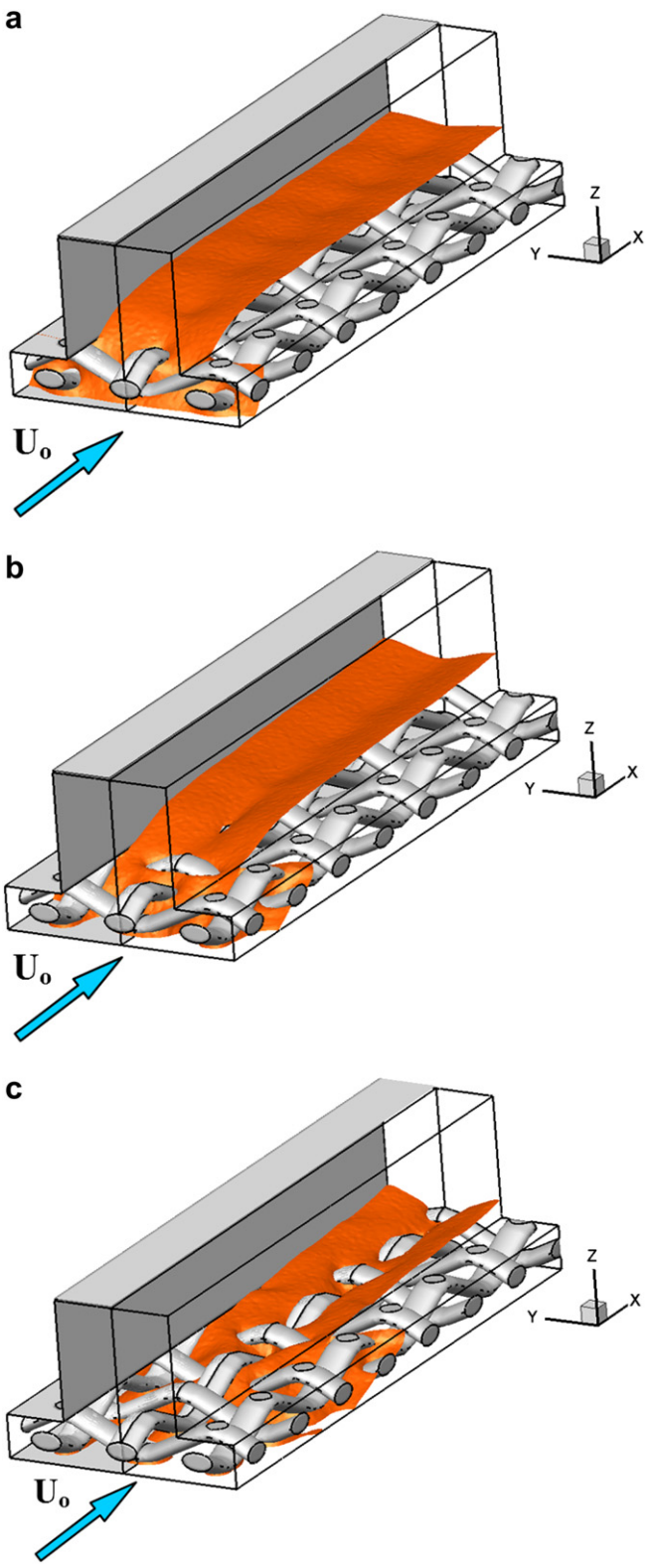

Fig. 13. Constant relative humidity condensation ($\varphi = 100\%$) iso-surfaces for $\varphi_{in} = 99.6\%$, $T_{in} = T_{membrane} = 353$ K, and a) $U_o = 0.3$ ms^{-1}, b) $U_o = 1.43$ ms^{-1} and c) $U_o = 4.3$ ms^{-1}. (Domain has been mirrored across XZ plane and the bipolar plate walls removed, for clarity).

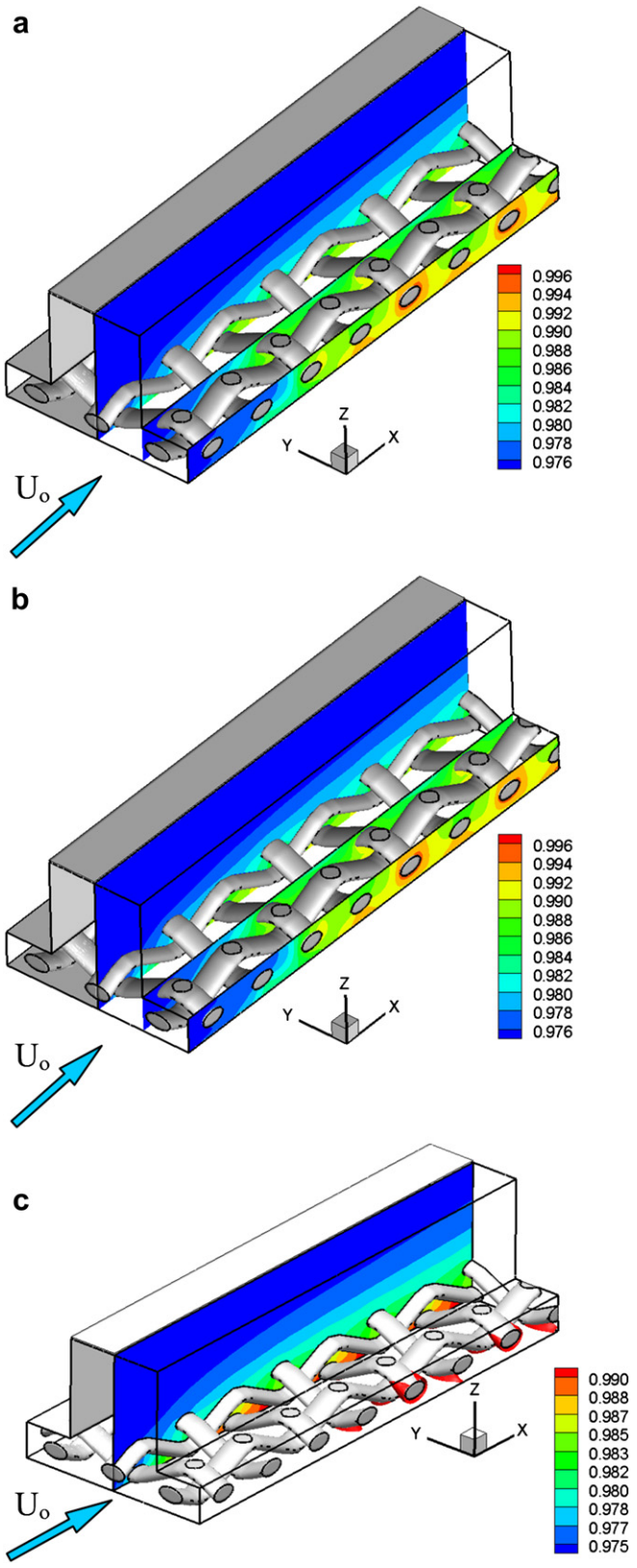

Fig. 14. a) Constant relative humidity contours on planes parallel to the main flow direction for $U_o = 1.43$ ms^{-1}, $T_{in} = T_{membrane} = 353$ K and $\varphi_{in} = 99.6\%$, b) Constant relative humidity contours on planes parallel to the main flow direction for $U_o = 1.43$ ms^{-1}, $T_{in} = T_{membrane} = 353$ K and $\varphi_{in} = 97\%$ and c) Iso-surfaces of maximum local relative humidity values - precursors of first condensation spots for $U_o = 1.43$ ms^{-1}, $T_{in} = T_{membrane} = 353$ K and $\varphi_{in} = 97\%$.

properties (graphite and ELAT) were also considered for the fibres. Humidity production and temperature at the catalyst layer was assumed to be constant for all cases. As previously stated, the set inlet parameters may be thought of as representative of a downstream position in the fuel cell's serpentine channel. Fig. 13 presents iso-surfaces of 100% relative humidity (condensation front) below which condensation is predicted to have occurred. Phase change is not considered here so the condensation front is indicative of the region where condensation will form. The effect of liquid water on the flow cannot be predicted within the scope of this investigation. It is obvious however that higher inlet velocities will delay condensation since the inlet air flow penetrates the cloth and it takes longer for the locally produced water vapour at the catalyst layer to provide the extra humidity needed for saturation of the incoming air. Temperature has no effect here since the inlet air is assumed to be at the catalyst temperature. When lower inlet temperatures where examined, representative condensation situations could not be attained since the higher catalyst layer temperature heated the air giving lower relative humidity values for the same humidity ratio. However, it is obvious from Fig. 13 that higher inlet velocities help in removing water vapour from the GDL and therefore delay the development of condensation conditions.

Fig. 14a and b show a comparison of constant humidity ratio contours for $\varphi_{in} = 99.6\%$ and 97% respectively ($U_o = 1.43$ ms^{-1}). At the lower inlet humidity value, condensation does not appear but the maximum values are indicative precursors. A clearer view is presented with iso-surfaces in Fig. 14c. Results show that the areas most favourable for condensation are in the constriction under the bipolar plate and between fibres and the membrane. These are actually regions that are farthest from the influence of the channel—in the Y direction—and far enough downstream for water vapour to build up.

Velocity effects can be quantified using the effective diffusion coefficient [12]. Due to the presence of the carbon cloth as well as the convective effects of the flow through the channel, this does not represent diffusion alone but can be used to compare the effective transport of water vapour compared to pure diffusion. The effective diffusion coefficient is defined as [12]:

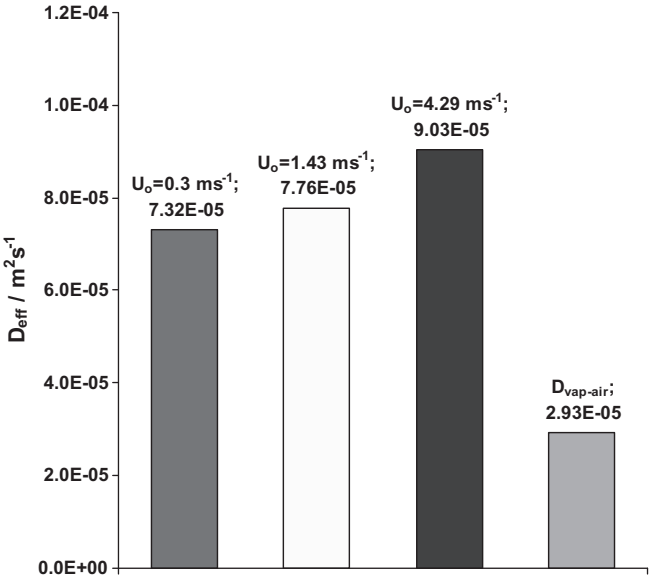

Fig. 15. Comparison of effective water vapour–air diffusion coefficients for various channel flow velocities and comparison to the value for water vapour diffusion in air.

$$D_{eff-vap} = \frac{1}{Z_{th}} \frac{\dot{m}_{H2O}/A_{cell}}{\left\{ \left[\rho_{mix}\left(\frac{W}{1+W}\right)\right]_{GDL} - \left[\rho_{mix}\left(\frac{W}{1+W}\right)\right]_{memb} \right\}} \quad (17)$$

where (ρ_{mix}) is the density of humid air, W is the humidity ratio, $\dot{m}_{H2O}$ is the water production at the membrane and A_{cell} is the membrane area in the computational domain. The denominator is actually the water vapour concentration gradient calculated from the mean concentration values at the membrane plane and the plane that defines the top of the cloth. Since water production is an imposed boundary condition in this work, the effective diffusion coefficient is actually solely dependent on the concentration gradient but it is interesting to compare it to the value of $D_{air\text{-}vap} = 2.93 \cdot 10^{-5}$ m^2 s^{-1} given by Quick et al. [12] for water vapour in air at 60 °C. Results are presented in Fig. 15 for various inlet velocities and at inlet temperatures equal to that of the catalyst, in order to include only the effects of the water production on the concentration gradient. Even at the lowest velocity values, vapour transport is increased compared to pure diffusion and as velocities increase, convective effects dominate and the effective diffusion coefficient increases significantly.

5. Conclusions

A 3D model simulating the pore scale topology of PEM cathode channel and GDL, including the carbon cloth structure has been presented. Heat and mass transfer have been solved for a range of inlet velocities as well as different cloth fibre material properties, using a conjugate heat transfer approach. Water vapour production at the catalyst layer is included in the calculations and its transport through the GDL is combined with psychrometric calculations to provide indications of the conditions and areas most prone to condensation i.e. where liquid formation originates.

In its present state, the numerical model is not in a position to provide for simulations of a PEM fuel cell's performance; indeed, there are a number of physical mechanisms missing: anode geometry, membrane, bipolar plates and cooling system, larger serpentine channel geometry, electrochemical phenomena etc. The study is an attempt to look at the pore scale heat and fluid flow phenomena in the GDL, while taking into account the fact that it belongs to a larger system. However, the computational effort that has been put into the pore scale has necessarily put some limitations on the modelling effort e.g. inclusion of the bipolar plates would be relatively simple with conjugate heat transfer but it would greatly increase both memory and computing time requirements. Also, modelling for voltage-current production and chemical reactions for a larger portion of the fuel cell channels may be too demanding computationally.

However, the results from the heat and mass transfer simulation may provide important insight for use in simpler models of the whole system. It has been shown that the assumption of constant GDL temperature as well as the choice of GDL material properties has a significant effect on the prediction of condensation and/or hot spot formation. Furthermore, the details of the heat and fluid flow interaction with local geometry, which determine where saturation first appears may aid in the channel geometry design procedure.

Acknowledgements

This research was funded under the operational program "Competitiveness" of the Greek Ministry of Development (Community Support Framework 2000–2006), as approved by the General Secretariat for Research and Technology (PENED 2003, 03ED902) and by Fluid Research Co.

References

[1] T.A. Trabold, J.P. Owejan, D.L. Jacobson, M. Arif, P.R. Huffman, In-situ investigation of water transport in an operating PEM fuel cell using neutron radiography. Part 1—experimental method and serpentine flow field results, Int. J. Heat Mass Trans. 49 (2006) 4712–4720.
[2] J.P. Owejan, T.A. Trabold, D.L. Jacobson, D.R. Baker, D.S. Hussey, M. Arif, In-situ investigation of water transport in an operating PEM fuel cell using neutron radiography. Part 2—transient water accumulation in an interdigitated cathode flow field, Int. J. Heat Mass Trans. 49 (2006) 4721–4731.
[3] J.P. Owejan, T.A. Trabold, D.L. Jacobson, M. Arif, S.G. Kandlikar, Effects of flowfield and diffusion layer properties on water accumulation in a PEM fuel cell, Int. J. Hydrogen. Energy. 32 (2007) 4489–4502.
[4] M. Grujicic, K.M. Chittajallu, Optimization of the cathode geometry in polymer electrolyte membrane (PEM) fuel cells, Chem. Eng. Sci. 59 (2004) 5883–5895.
[5] P. Quan, M.C. Lai, Numerical study of water management in the air flow channel of a PEM fuel cell cathode, J. Power Sources 164 (2007) 222–237.
[6] P.M. Kumar, A.K. Kolar, Effect of cathode channel dimensions on the performance of an air-breathing PEM fuel cell, Int. J. Thermal Sci. 49 (2010) 844–857.
[7] A. Su, F.B. Weng, C.Y. Hsu, Y.M. Chen, Studies on flooding in PEM fuel cell cathode channels, Int. J. Hydrogen. Energy. 31 (2006) 1031–1039.
[8] P.T. Nguyen, T. Berning, N. Djilali, Computational model of a PEM fuel cell with serpentine gas flow channels, J. Power Sources 130 (2004) 149–157.
[9] Y. Zong, B. Zhou, A. Sobiesiak, Water and thermal management in a single PEM fuel cell with non-uniform stack temperature, J. Power Sources 161 (2006) 143–159.
[10] M. Khandelwal, M.M. Mench, Direct measurement of through-plane thermal conductivity and contact resistance in fuel cell materials, J. Power Sources 161 (2006) 1106–1115.
[11] J.H. Nam, K.J. Lee, G.S. Hwang, C.J. Kim, M. Kaviany, Microporous layer for water morphology control in PEMFC, Int. J. Heat Mass Transfer 52 (2009) 2779–2791.
[12] C. Quick, D. Ritzinger, W. Lehnert, C. Hartnig, Characterization of water transport in gas diffusion media, J. Power Sources 190 (1) (2009) 110–120.
[13] N.P. Siegel, M.W. Ellis, D.J. Nelson, M.R. von Spakovsky, Single domain PEMFC model based on agglomerate catalyst geometry, J. Power Sources 115 (2003) 81–89.
[14] A. Theodorakakos, T. Ous, M. Gavaises, J.M. Nouri, N. Nikolopoulos, H. Yanagihara, Dynamics of water droplets detached from porous surfaces of relevance to PEM fuel cells, Int. J. Colloids Interface Sci. 300 (2) (2006) 673–687.
[15] T. Ous, C. Arcoumanis, Visualisation of water droplets during the operation of PEM fuel cells, J. Power Sources 173 (1) (2007) 137–148.
[16] T. Ous, C. Arcoumanis, Visualisation of water accumulation in the flow channels of PEMFC under various operating conditions, J. Power Sources 187 (1) (2009) 182–189.
[17] S.Y. Yoon, J.W. Ross, M.M. Mench, K.V. Sharp, Gas-phase particle image velocimetry (PIV) for application to the design of fuel cell reactant flow channels, J. Power Sources 160 (2) (2006) 1017–1025.
[18] P.P. Mukherjee, C.Y. Wang, Stochastic microstructure reconstruction and direct numerical simulation of the PEFC catalyst layer, J. Electrochem. Soc. 153 (2006) A840–A849.
[19] B.V. Kasula, L. Mercado, P. Asinari, M.R. von Spakovsky, 3D microstructure reconstructions of solid oxide and proton exchange membrane fuel cell electrodes with applications to numerical simulations of reacting mixture flows using LBM, in, Proc. ASME Int. Mech. Eng. Congress Exposition 6 (2008) 643–654.
[20] G. Inoue, T. Yoshimoto, Y. Matsukuma, M. Minemoto, Development of simulated gas diffusion layer of polymer electrolyte fuel cells and evaluation of its structure, J. Power Sources 175 (2008) 145–158.
[21] J.W. Park, K. Jiao, X. Li, Numerical investigations on liquid water removal from the porous gas diffusion layer by reactant flow, Appl. Energy Press. (2010). doi:10.1016/j.apenergy.2009.11.021.
[22] Kopanidis A., Theodorakakos A., Gavaises E., Bouris D., Direct Modelling of the Microscale Flow through a PEM Fuel Cell GDL and Channel, in: S. Colin, G.L. Morini, Proceedings of the first European Conference on Microfluidics, Bologna, Italy, (2008), μFlu'08–180.
[23] Siegel N.P., Development and validation of a computational model for a proton exchange membrane fuel cell, PhD thesis (2003) Virginia Polytechnic Institute and State University.
[24] J.P. Feser, A.K. Prasad, S.G. Advani, Experimental characterization of in-plane permeability of gas diffusion layers, J. Power Sources 162 (2006) 1226–1231.
[25] I. Verpoest, S.V. Lomov, Virtual textile composites software Wisetex: integration with micro-mechanical, permeability and structural analysis, Comp. Sci. Technol. 65 (15–16) (2005) 2563–2574.
[26] R. Roshandel, B. Farhanieh, E. Saievar-Iranizad, The effects of porosity distribution variation on PEM fuel cell performance, Renewable Energy 30 (2005) 1557–1572.
[27] S.V. Patankar, B.D. Spalding, A calculation procedure for heat, mass and momentum transfer in three-dimensional parabolic flows, Int. J. Heat Mass Transfer 15 (1972) 1787–1806.
[28] A. Kopanidis, A. Theodorakakos, E. Gavaises, D. Bouris, 3D numerical simulation of flow and conjugate heat transfer through a pore scale model of open cell metal foam, Int. J. Heat Mass Transfer 53 (11-12) (2010) 2539–2550.
[29] D. Bolton, The Computation of equivalent potential temperature, Monthly Weather Rev. 108 (1980) 1046–1053.

[30] R.W. Hyland, A. Wexler, Formulations for the thermodynamic properties of the saturated phases of H_2O from 173.15 K to 473.15 K, ASHRAE Transactions 89 (2A) (1983) 500–519.
[31] ASHRAE, Handbook, Fundamentals, SI Edition. Ashrae, 2009, ISBN 978-1-933742-55-7.
[32] Y.O. Devres, Psychrometric properties of humid air: calculation procedures, Appl. Energy 48 (1994) 1–18.
[33] P. Quan, B. Zhou, A. Sobiesiak, Z. Liu, Water behavior in serpentine micro-channel for proton exchange membrane fuel cell cathode, J. Power Sources 152 (2005) 131–145.
[34] M.H. Chang, F. Chen, H.S. Teng, Effects of two-phase transport in the cathode gas diffusion layer on the performance of a PEMFC, J. Power Sources 160 (2006) 268–276.
[35] S.G. Kandlikar, Z. Lu, Thermal management issues in a PEMFC stack–A brief review of current status, Appl. Thermal Eng. 29 (2009) 1276–1280.
[36] J. Yuan, M. Rokni, B. Sunden, A numerical investigation of gas flow and heat transfer in proton exchange membrane fuel cells, Numer. Heat Transfer Part A 44 (2003) 255–280.
[37] I.S. Hussaini, C.Y. Wang, Visualization and quantification of cathode channel flooding in PEM fuel cells, J. Power Sources 187 (2009) 444–451.
[38] J. Ramousse, S. Didierjean, O. Lottin, D. Maillet, Estimation of the effective thermal conductivity of carbon felts used as PEMFC Gas Diffusion Layers, Int. J. Thermal Sci. 47 (2008) 1–6.
[39] E. Kikkinides, D. Bouris, D. Tsiplakides, G. Marnellos, E. Smotkin, Understanding Microscale Mechanisms in the Cathode Gas Diffusion Layer Of Proton Exchange Membrane Fuel Cells (2006–2008). General Secreteriat for Research and Technology, Ministry of Development, 2008, Greece–USA Collaboration–Final Report.
[40] J. Larminie, A. Dick, Fuel Cell Systems Explained. Wiley, 2003, ISBN 0470 84857X.
[41] A.S. Rawool, S.K. Mitra, J.G. Pharoah, An investigation of convective transport in micro proton-exchange membrane fuel cells, J. Power Sources 162 (2006) 985–991.
[42] M. Coppo, N.P. Siegel, M.R. von Spakovsky, On the influence of temperature on PEM fuel cell operation, J. Power Sources 159 (2006) 560–569.
[43] P.C. Sui, S. Kumar, N. Djilali, Advanced computational tools for PEM fuel cell design Part 2. Detailed experimental validation and parametric study, J. Power Sources 180 (2008) 423–432.
[44] J.E. Dawes, N.S. Hanspal, O.A. Family, A. Turan, Three-dimensional CFD modelling of PEM fuel cells: an investigation into the effects of water flooding, Chem. Eng. Sci. 64 (2009) 2781–2794.